

Air Force Institute of Technology

AFIT Scholar

Faculty Publications

7-2019

Nondestructive Electromagnetic Characterization of Uniaxial Sheet Media Using a Two-Flanged Rectangular Waveguide Probe

Neil G. Rogers

Michael J. Havrilla

Air Force Institute of Technology

Milo W. Hyde IV

Air Force Institute of Technology

Alexander G. Knisely

Follow this and additional works at: <https://scholar.afit.edu/facpub>



Part of the [Electromagnetics and Photonics Commons](#)

Recommended Citation

N. Rogers, M. Havrilla, M. W. Hyde and A. Knisely, "Nondestructive Electromagnetic Characterization of Uniaxial Sheet Media Using a Two-Flanged Rectangular Waveguide Probe," in *IEEE Transactions on Instrumentation and Measurement*, vol. 69, no. 6, pp. 2938-2947, June 2020, doi: <https://10.1109/TIM.2019.2925408>.

This Article is brought to you for free and open access by AFIT Scholar. It has been accepted for inclusion in Faculty Publications by an authorized administrator of AFIT Scholar. For more information, please contact richard.mansfield@afit.edu.

Nondestructive Electromagnetic Characterization of Uniaxial Sheet Media Using a Two-Flanged Rectangular Waveguide Probe

Neil Rogers, Michael Havrilla, *Member, IEEE*, Milo Hyde, *Member, IEEE*, and Alexander Knisely

I. INTRODUCTION

RECENT advancements in fabrication capabilities have renewed interest in the electromagnetic characterization of complex media, as many metamaterials are anisotropic and/or inhomogeneous. Additionally, for composite materials, anisotropy can be introduced by load, strain, misalignment, or damage through the manufacturing process [1], [2]. Methods for obtaining the constitutive parameters for isotropic materials are well understood and widely employed [3]–[8]. Therefore, it is crucial to develop a practical method for the electromagnetic characterization of anisotropic materials.

Characterization methods for anisotropic media are significantly more difficult, due to the inherent complexity of the resultant form of Maxwell’s equations and the requirement for a greater number of measurements. Destructive, free space, and cavity methods, such as those detailed in [9]–[16] can be very useful, but require a precisely cut sample, which is not always available for many practical scenarios. Recently, the two-flanged waveguide measurement technique (tFWMT) employed in [5], [8], [17] has been demonstrated effectively in extracting both permittivity (ϵ_r) and permeability (μ_r) of isotropic materials. Additionally, the coaxial clamped probe (CCP) method was employed [18] in extracting the constitutive parameters of anisotropic materials. However, due to well-known issues with characterizing low-permittivity materials, the uncertainty associated with the CCP method is greater than that of the tFMWT.

This paper advances the state-of-the-art with regards to non-destructive electromagnetic characterization by extending the theory of the tFMWT to account for uniaxial anisotropy and furthermore presents the significant result of demonstrating the method experimentally. It is shown the present method reduces much of the uncertainty associated with the CCP, but maintaining similar accuracy. Additionally, this work provides a promising foundation for the electromagnetic characterization of more general classes of complex media, such as gyrotropic.

Manuscript received 30 Sept 2018; revised 15 June 2019. The views expressed in this paper are those of the authors and do not reflect the official policy or position of the U.S. Air Force, the Department of Defense, or the U.S. Government.

N. Rogers, M. Havrilla, M. Hyde, and Alexander Knisely are with the Department of Electrical and Computer Engineering, Air Force Institute of Technology, WPAFB, OH, 45433. E-mail: neil.rogers@us.af.mil

The theoretical development of the tFWMT for uniaxial media, is presented in the first section. Following the previous work, this analysis focuses on the derivation of the theoretical scattering parameters for uniaxial media, which are ultimately required for permittivity and permeability extraction. These parameters are formulated by first applying Love’s equivalence principle and then enforcing the continuity of tangential fields. The resulting coupled system of Magnetic Field Integral Equations (MFIEs) is subsequently solved for the theoretical scattering parameters using the Method of Moments (MoM). Lastly, the desired complex permittivity and permeability tensor elements are determined via a nonlinear least squares minimization of the difference between the theoretical and measured scattering parameters.

To validate the new tFWMT, experimental results of two non-magnetic honeycomb materials are presented in Section III. The permittivity tensor results obtained using the extended tFWMT are compared with those obtained using a traditional destructive characterization method. The tFMWT’s sensitivities to common experimental errors are also investigated.

II. TWO-FLANGED WAVEGUIDE MEASUREMENT TECHNIQUE

In general, the complex permittivity and permeability tensor elements, $\vec{\epsilon} = \hat{x}\hat{x}\epsilon_t + \hat{y}\hat{y}\epsilon_t + \hat{z}\hat{z}\epsilon_z$ and $\vec{\mu} = \hat{x}\hat{x}\mu_t + \hat{y}\hat{y}\mu_t + \hat{z}\hat{z}\mu_z$, can be determined via a nonlinear least squares minimization of the difference between the theoretical and experimental scattering parameters:

$$\arg \min_{\epsilon_t, \epsilon_z, \mu_t, \mu_z \in \mathbb{C}} \left\| \begin{bmatrix} S_{11}^{\text{thy}}(f, d; \epsilon_t, \epsilon_z, \mu_t, \mu_z) - S_{11}^{\text{exp}}(f) \\ S_{21}^{\text{thy}}(f, d; \epsilon_t, \epsilon_z, \mu_t, \mu_z) - S_{21}^{\text{exp}}(f) \\ S_{12}^{\text{thy}}(f, d; \epsilon_t, \epsilon_z, \mu_t, \mu_z) - S_{12}^{\text{exp}}(f) \\ S_{22}^{\text{thy}}(f, d; \epsilon_t, \epsilon_z, \mu_t, \mu_z) - S_{22}^{\text{exp}}(f) \end{bmatrix} \right\|_2, \quad (1)$$

where f is the frequency and d is the thickness of the material under test (MUT). Note, in the case of Figure 1, S_{11} is not independent from S_{22} , nor is S_{21} independent from S_{12} , therefore only enough independent measurements are available to extract two of the four uniaxial constitutive parameters. The dependent measurements are included to minimize experimental errors. In order to extract all four parameters, an additional set of independent measurements is necessary. For

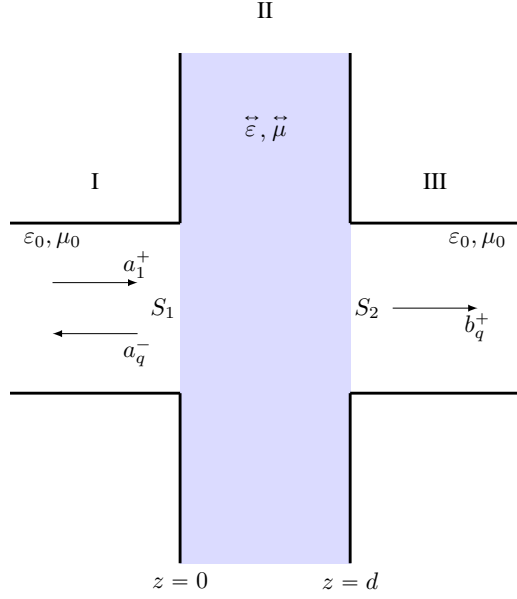


Figure 1: Geometry of the tFWMT. The MUT, of thickness d and parameters $\vec{\epsilon}$ and $\vec{\mu}$, is clamped between two free-space-filled infinitely-flanged $a \times b$ rectangular waveguides. The complex amplitudes of the incident mode, the reflected modes, and the transmitted modes are specified by a_1^+ , a_q^- and b_q^+ , respectively.

some materials, a two-thickness method (TTM) [3] could be used (when a suitable second thickness of the MUT is available) or the two-layer method (TLM) [19].

In developing the theoretical coefficients, Love's equivalence principle, continuity of tangential fields, and the MoM are utilized to arrive at a set of coupled MFIEs. The MFIEs contain six integrals, which if calculated numerically, would require tremendous computational resources given the number of function evaluations required by the nonlinear least squares solver. Therefore, the integrals are evaluated in the spectral domain using complex plane analysis resulting in a single remaining integral which is evaluated numerically.

A. MFIE development and MoM solution

The physical configuration of the tFWMT geometry is shown in Fig. 1. The first step in developing the MFIEs is to determine the fields in each region (I, II, and III). Since boundary conditions are enforced at $z = 0$ and $z = d$, only the tangential fields, indicated by the subscript t , are reported here. The tangential fields in Regions I and III are

$$\begin{aligned} \vec{E}_{t,I} &= a_1^+ \vec{e}_1 e^{-\gamma_1 z} + \sum_{q=1}^Q a_q^- \vec{e}_q e^{\gamma_q z} \\ \vec{H}_{t,I} &= a_1^+ \vec{h}_1 e^{-\gamma_1 z} - \sum_{q=1}^Q a_q^- \vec{h}_q e^{\gamma_q z} \end{aligned} \quad (2)$$

and

$$\begin{aligned} \vec{E}_{t,III} &= \sum_{q=1}^Q b_q^+ \vec{e}_q e^{-\gamma_q(z-d)} \\ \vec{H}_{t,III} &= \sum_{q=1}^Q b_q^+ \vec{h}_q e^{-\gamma_q(z-d)} \end{aligned}, \quad (3)$$

where q represents the mode index (m, n combination), \vec{e}_q and \vec{h}_q are the tangential components of the rectangular waveguide electric and magnetic field distributions (both TE^z and TM^z), respectively [20], and $\gamma_q = \sqrt{(m\pi/a)^2 + (n\pi/b)^2 - k_0^2}$. Here, $k_0 = \omega\sqrt{\epsilon_0\mu_0}$ is the free-space wavenumber and $\omega = 2\pi f$. Note that the tFWMT symmetry condition discussed in [5] holds here. Therefore, $q = 1$ describes the TE_{10}^z mode, $q = 2$ describes the TE_{30}^z mode, etc. A list of the first 20 values of q and the corresponding modes is given in [21].

In anticipation of enforcing the continuity of tangential fields and a subsequent MoM solution, the electric field given in (2) is evaluated at $z = 0$ (denoted by \vec{e}_{a1}) and tested using the q^{th} mode of the electric field. Rearranging (2) and utilizing mode orthogonality, one obtains

$$a_q^- = \int_{S_1} \vec{e}_q \cdot \vec{e}_{a1} dS - a_1^+ \delta_{q1} \quad (4)$$

with

$$\delta_{q1} = \begin{cases} 1 & \dots q = 1 \\ 0 & \dots q \neq 1 \end{cases}. \quad (5)$$

Performing similar operations on the electric field of (3) evaluated at $z = d$ (denoted by \vec{e}_{a2}), one finds

$$b_q^+ = \int_{S_2} \vec{e}_q \cdot \vec{e}_{a2} dS. \quad (6)$$

Substituting (4) and (6) into the magnetic fields of Regions I and III evaluated at $z = 0$ and $z = d$, respectively, yields

$$\vec{H}_{t,I}(z = 0) = 2a_1^+ \vec{h}_1 - \sum_{q=1}^Q \left(\int_{S_1} \vec{e}_q \cdot \vec{e}_{a1} dS \right) \vec{h}_q \quad (7)$$

$$\vec{H}_{t,III}(z = d) = \sum_{q=1}^Q \left(\int_{S_2} \vec{e}_q \cdot \vec{e}_{a2} dS \right) \vec{h}_q. \quad (8)$$

Next, an expression is obtained for the tangential magnetic field in the parallel-plate region of the tFWMT (Region II). This expression is given in the familiar Green's function form via Love's equivalence principle:

$$\vec{H}_t^{\text{pp}}(\vec{\rho}, z) = \sum_{c=1}^2 \int_{S'_c} \vec{G}_{hh}(\vec{\rho}, z | \vec{\rho}'_c, z'_c) \cdot \vec{J}_{hc}(\vec{\rho}'_c, z'_c) dS'_c. \quad (9)$$

Defining $\vec{\lambda}_\rho = \hat{x}\lambda_x + \hat{y}\lambda_y$ and $d^2\lambda_\rho = d\lambda_x d\lambda_y$, the dyadic spatial-domain Green's function of (9) is the inverse transform of the spectral-domain Green's function, which is given explicitly in [22]:

$$\begin{aligned} & \vec{G}_{hh}(\vec{\rho}, z|\vec{\rho}', z') \\ &= \frac{1}{4\pi^2} \iint_{-\infty}^{\infty} \vec{\tilde{G}}_{hh}(\vec{\lambda}_\rho, z|z') e^{j\vec{\lambda}_\rho \cdot (\vec{\rho} - \vec{\rho}')} d^2\lambda_\rho \end{aligned} \quad (10)$$

with $\vec{J}_{h1} = -\hat{z} \times \vec{e}_{a1}$ and $\vec{J}_{h2} = \hat{z} \times \vec{e}_{a2}$.

In the summation notation used in (9), the c index refers to the aperture under consideration. Note that because the tFWM is a two-port device, there will be a ‘‘self’’ term and a ‘‘cross’’ term to account for the two source and observation points ($z, z' = 0$ and $z, z' = d$). Here, the unprimed coordinates correspond to the observation points, while the primed coordinates refer to the location of the source. The single overset tilde represents a quantity that has been Fourier transformed on the transverse spatial variables, x and y . The first h in the hh subscript on the Green's function refers to the observed transverse magnetic field, while the second h refers to the source which maintains the field—an equivalent transverse magnetic surface current in this case.

Finally, enforcing the continuity of the tangential magnetic fields at $z = 0$ and $z = d$ leads to the desired system of coupled MFIEs:

$$2a_1^+ \vec{h}_1 - \sum_{q=1}^Q \left(\int_{S_1} \vec{e}_q \cdot \vec{e}_{a1} dS \right) \vec{h}_q = \sum_{c=1}^2 (-1)^c \frac{1}{4\pi^2} \Theta_{1c} \quad (11)$$

and

$$\sum_{q=1}^Q \left(\int_{S_2} \vec{e}_q \cdot \vec{e}_{s2} dS \right) \vec{h}_q = \sum_{c=1}^2 (-1)^c \frac{1}{4\pi^2} \Theta_{2c}, \quad (12)$$

where

$$\begin{aligned} \Theta_{1c} = & \iint_{-\infty}^{\infty} \left\{ \int_0^b \int_0^a \vec{\tilde{G}}_{hh}(\vec{\lambda}_\rho, z_1^+|z_c') \cdot [\hat{z} \times \vec{e}_{ac}(\vec{r}'_c)] \right. \\ & \left. e^{j\vec{\lambda}_\rho \cdot (\vec{\rho} - \vec{\rho}')} dx' dy' \right\} d^2\lambda_\rho \end{aligned} \quad (13)$$

and

$$\begin{aligned} \Theta_{2c} = & \iint_{-\infty}^{\infty} \left\{ \int_0^b \int_0^a \vec{\tilde{G}}_{hh}(\vec{\lambda}_\rho, z_2^-|z_c') \cdot [\hat{z} \times \vec{e}_{ac}(\vec{r}'_c)] \right. \\ & \left. e^{j\vec{\lambda}_\rho \cdot (\vec{\rho} - \vec{\rho}')} dx' dy' \right\} d^2\lambda_\rho \end{aligned} \quad (14)$$

In Θ_{1c} and Θ_{2c} , z_1^+ is the position just to the right of $z = 0$ and z_2^- is the position just to the left of $z = d$. The subscript index c denotes the appropriate aperture for the source terms. Furthermore, throughout this paper, primed variables correlate with source terms and unprimed variables correlate with observation terms. The MoM is used to solve

the above system of MFIEs. The unknown aperture electric fields are expanded using the tangential rectangular waveguide electric field distributions given in (2) and (3), namely

$$\begin{aligned} \vec{e}_{a1} &= \sum_{w=1}^W a_1^+ C_w^{(1)} \vec{e}_w \\ \vec{e}_{a2} &= \sum_{w=1}^W a_1^+ C_w^{(2)} \vec{e}_w \end{aligned} \quad (15)$$

Note that the generic mode index q has been replaced with a mode index w , which refers specifically to the basis functions to represent the TE^{*z*}/TM^{*z*} modes. As was previously mentioned, $w = 1$ refers to the TE₁₀ mode, $w = 2$ refers to the TE₃₀ mode, etc. Furthermore, in some cases it is necessary to distinguish between whether the x and y variations in the modes, which are typically denoted by m and n , are specifically associated with the testing or basis functions. In these cases, the testing functions are designated by the notation TE/TM^{*z*}_{*m_vn_v*} and the basis functions by the notation TE/TM^{*z*}_{*m_wn_w*}. The resulting equations are then tested using the tangential rectangular waveguide magnetic field distributions also provided in (2) and (3). In this case, v is used as the mode index for the testing modes, namely,

$$\begin{aligned} & \int_{S_1} \vec{h}_v(\vec{\rho}_1) \cdot \left\{ (11) \right\} dS_1 \\ & \int_{S_2} \vec{h}_v(\vec{\rho}_2) \cdot \left\{ (12) \right\} dS_2 \end{aligned}, \quad (16)$$

where the expansion indices represent the total number of modes considered, thus determining the accuracy of the theoretical solution. After applying the testing and expansion functions, a $2Q \times 2Q$ system of equations is formed, namely,

$$\underbrace{\begin{bmatrix} A^{(11)} & A^{(12)} \\ A^{(21)} & A^{(22)} \end{bmatrix}}_{2Q \times 2Q} \underbrace{\begin{bmatrix} C^{(1)} \\ C^{(2)} \end{bmatrix}}_{2Q \times 1} = \underbrace{\begin{bmatrix} B^{(1)} \\ B^{(2)} \end{bmatrix}}_{2Q \times 1}, \quad (17)$$

where:

$$\begin{aligned}
 A_{vw}^{(11)} &= \int_{S_1} \vec{h}_v(\vec{r}_1) \cdot \vec{h}_w(\vec{r}_1) dS_1 \\
 &\quad - \frac{Z_w}{4\pi^2} \iint_{-\infty}^{\infty} \left(\vec{\Lambda}_{v,1} \cdot \vec{G}_{hh}(\vec{\lambda}_\rho, z_1 | z'_1) \cdot \vec{\Lambda}_{w,1} \right) d^2\lambda_\rho \\
 A_{vw}^{(12)} &= \frac{Z_w}{4\pi^2} \iint_{-\infty}^{\infty} \left(\vec{\Lambda}_{v,1} \cdot \vec{G}_{hh}(\vec{\lambda}_\rho, z_1 | z'_2) \cdot \vec{\Lambda}_{w,2} \right) d^2\lambda_\rho \\
 B^{(1)} &= 2 \int_{S_1} \vec{h}_v(\vec{r}_1) \cdot \vec{h}_1(\vec{r}_1) dS_1 \\
 B^{(2)} &= 0 \\
 \vec{\Lambda}_{v,\alpha} &= \int_0^b \int_0^a \vec{h}_v(\vec{r}'_\alpha) e^{j\vec{\lambda}_\rho \cdot \vec{\rho}} dx dy \\
 \vec{\Lambda}_{w,\alpha} &= \int_0^b \int_0^a \vec{h}_w(\vec{r}'_\alpha) e^{-j\vec{\lambda}_\rho \cdot \vec{\rho}'} dx' dy'
 \end{aligned} \tag{18}$$

Here, the double integrals depicted by the Λ notation represent the total observed (unprimed variables) and source (primed variables) magnetic fields at a given aperture (α subscript). Furthermore, the Z_w terms represent the wave (and mode) impedance for the waveguide region. Note that $\alpha = 1, 2$ and $A_{vw}^{(22)} = A_{vw}^{(11)}$, $A_{vw}^{(21)} = A_{vw}^{(12)}$ due to the symmetry of the tFWMT and electromagnetic reciprocity, respectively.

Solving for \vec{C} in (17) leads to the theoretical scattering coefficients necessary to solve (1) via nonlinear least squares. The theoretical scattering coefficients are found from the MoM expansion coefficients, (4) and (6), by

$$S_{11}^{\text{thy}} = \frac{a_1^-}{a_1^+} = C_1^{(1)} - 1 \tag{19}$$

$$S_{21}^{\text{thy}} = \frac{b_1^+}{a_1^+} = C_1^{(2)}, \tag{20}$$

where the theoretical transmission and reflection coefficients are found from the first element in each subarray of \vec{C} , which corresponds to the dominant propagation mode in the waveguide. Note, solution convergence is typically reached using a small number, Q , of higher-order modes.

B. Evaluation of the λ_y integral via complex plane analysis

Although a complete solution to the minimization problem in (1) has been determined, the solution may be expedited considerably by the analytical evaluation of some of the integrals of (18). Evaluation of the $\vec{\Lambda}_v$ and $\vec{\Lambda}_w$ spatial integrals over the observation variables x and y and the source variables x' and y' , respectively, is very straightforward. Furthermore, in one of the main departures from the isotropic case, the

Green's function is a dyad with off-diagonal elements, thereby requiring expansion of the dot products. Here, the MoM matrix elements $A_{vw}^{(11)}$ are evaluated. The evaluation of the others follows in a similar manner.

After evaluating the $\vec{\Lambda}_v$ and $\vec{\Lambda}_w$ spatial integrals, $A_{vw}^{(11)}$ takes the form

$$\begin{aligned}
 A_{vw}^{(11)} &= \delta_{v,w} \left(\frac{ab}{4} \right) \left[(M_{xv}^h)^2 + (M_{yv}^h)^2 \right] (1 + \delta_{w,m,0}) \\
 &\quad - \frac{Z_w}{4\pi^2} \int_{-\infty}^{\infty} \left\{ A_{\lambda_x}^{(11)} \int_{-\infty}^{\infty} \left[M_{xv}^h M_{xw}^h k_{xv} k_{xw} \lambda_y^2 \tilde{G}_{hh,xx}^{00} \right. \right. \\
 &\quad + M_{xv}^h M_{yw}^h k_{xv} k_{yw} \lambda_x \lambda_y \tilde{G}_{hh,xy}^{00} \\
 &\quad + M_{yv}^h M_{xw}^h k_{xv} k_{yw} \lambda_x \lambda_y \tilde{G}_{hh,yx}^{00} \\
 &\quad \left. \left. + M_{yv}^h M_{yw}^h k_{yv} k_{yw} \lambda_x^2 \tilde{G}_{hh,yy}^{00} \right] A_{\lambda_y}^{(11)} d\lambda_y \right\} d\lambda_x
 \end{aligned} \tag{21}$$

with

$$A_{\lambda_x}^{(11)} = \frac{(1 - (-1)^{m_v} e^{j\lambda_x a}) (1 - (-1)^{m_w} e^{-j\lambda_x a})}{(\lambda_x + k_{xv}) (\lambda_x - k_{xv}) (\lambda_x + k_{xw}) (\lambda_x - k_{xw})} \tag{22}$$

$$A_{\lambda_y}^{(11)} = \frac{(1 - (-1)^{n_v} e^{j\lambda_y b}) (1 - (-1)^{n_w} e^{-j\lambda_y b})}{(\lambda_y + k_{yv}) (\lambda_y - k_{yv}) (\lambda_y + k_{yw}) (\lambda_y - k_{yw})}, \tag{23}$$

where the notation for the Green's functions has been condensed such that

$$\tilde{G}_{hh,xx}^{00} = \tilde{G}_{hh,xx}(z = 0 | z' = 0). \tag{24}$$

Here, the M and Z terms are dependent on whether the mode is TE^z or TM^z :

$$\begin{aligned}
 \dots \text{ for } \text{TE}_{m_\alpha n_\alpha}^z &\left\{ \begin{array}{l} M_{x\alpha}^h = k_{x\alpha} / Z_\alpha \\ M_{y\alpha}^h = k_{y\alpha} / Z_\alpha \\ Z_\alpha = j\omega\mu_0 / \gamma_{z\alpha} \end{array} \right. \\
 \dots \text{ for } \text{TM}_{m_\alpha n_\alpha}^z &\left\{ \begin{array}{l} M_{x\alpha}^h = k_{y\alpha} \\ M_{y\alpha}^h = -k_{x\alpha} \\ Z_\alpha = \gamma_{z\alpha} / (j\omega\epsilon_0) \end{array} \right. ,
 \end{aligned}$$

where $k_{x\alpha} = m_\alpha \pi / a$; $k_{y\alpha} = n_\alpha \pi / b$; and $\alpha = v, w$ (specifying the testing or basis functions, respectively). Additionally, since propagation in only the z -direction is assumed, γ_q has been written as $\gamma_{z\alpha}$, where, again, α specifies either the testing or basis mode.

In order to analytically evaluate the spectral-domain integrals, Cauchy's Integral Theorem (CIT), Jordan's Lemma, and Cauchy's Integral Formula (CIF) are utilized. It is shown that only one of the spectral integrals can be handled analytically, as a branch cut appears in the second integral which requires much more complicated analysis. Here, the λ_y integral is evaluated analytically; the λ_x integral is evaluated numerically.

Upon inspection of the $A_{vw}^{(11)}$ term, one notes that the poles located at $\pm k_{y\alpha}$ dictate how the λ_y integral must be evaluated—the other poles not being dependent on n_α . As such, five

possible cases manifest for (21) depending on the values of n_v and n_w :

- I $n_v = n_w = 0$
- II $n_v \neq 0, n_w = 0$
- III $n_v = 0, n_w \neq 0$
- IV $n_v = n_w \neq 0$
- V $n_v \neq n_w \neq 0$.

Each of these cases must be considered independently. This paper gives a short overview of the process for I, which contains the dominant mode-only assumption.

For I, $n_v = n_w = 0$, which leads to $k_{yv} = k_{yw} = 0$. Therefore, the λ_y integral of (21) simplifies to

$$\int_{-\infty}^{\infty} \left\{ \frac{M_{xv}^h M_{xw}^h k_{xv} k_{xw}}{\lambda_y^2} \left(\frac{j\lambda_{z\theta} \lambda_x^2}{\lambda_\rho^2 \omega \mu_t} \right) \left[\frac{\cos(\lambda_{z\theta} d)}{\sin(\lambda_{z\theta} d)} \right] \right. \\ \left. \left[(1 - e^{j\lambda_y b}) + (1 - e^{-j\lambda_y b}) \right] \right\} d\lambda_y \quad (25)$$

where $\lambda_{z\theta} = \sqrt{k_t^2 - \mu_t/\mu_z (\lambda_x^2 + \lambda_y^2)}$ and $k_t = \omega \sqrt{\varepsilon_t \mu_t}$. Examining the exponentials, one concludes that upper half plane (UHP) closure is required for the $\exp(j\lambda_y b)$ term, while lower half plane (LHP) closure is required for the other. Both cases are considered separately and combined for the final result. Additionally, the spectral-domain Green's function consists of a TE^z contribution and a TM^z contribution; these are also considered separately. For the sake of brevity, only the TE^z case in the UHP is considered here.

The complex plane contour used in evaluating (25) is drawn in Fig. 2. In the UHP, the semicircular contour C_R^+ is shown and its contribution to the overall integral is considered in the limit as $R \rightarrow \infty$. Note that the other poles arise from the spectral-domain Green's function, i.e., the poles at $\pm j\lambda_x$ and $\pm \sqrt{\mu_z/\mu_t [k_t^2 - (l\pi/d)^2] - \lambda_x^2}$. The CIT provides a means for calculating the value of (25) over a simply closed contour in the complex plane:

$$0 = \int_{-\infty}^{\infty} + \int_{C_0^+} + \oint_{C_{j\lambda_x}^+} + \oint_{\Sigma C_l^+} + \int_{C_\infty^+} \quad (26)$$

$$\int_{-\infty}^{\infty} = \oint_{C_0^+} + \oint_{C_{j\lambda_x}^+} + \oint_{\Sigma C_l^+} \quad (27)$$

$$= j\pi \text{Res}(\lambda_y = 0) + j2\pi \text{Res}(\lambda_y = j\lambda_x) \\ + j2\pi \sum_l \text{Res}(\lambda_{z\theta} = \pm \frac{\pi l}{d}) \quad (28)$$

where the contribution from $C_\infty^+ \rightarrow 0$ as $R \rightarrow \infty$, as stipulated by Jordan's lemma. The CIF is then employed to calculate the residue of each pole. Repeating this process for the TE^z LHP

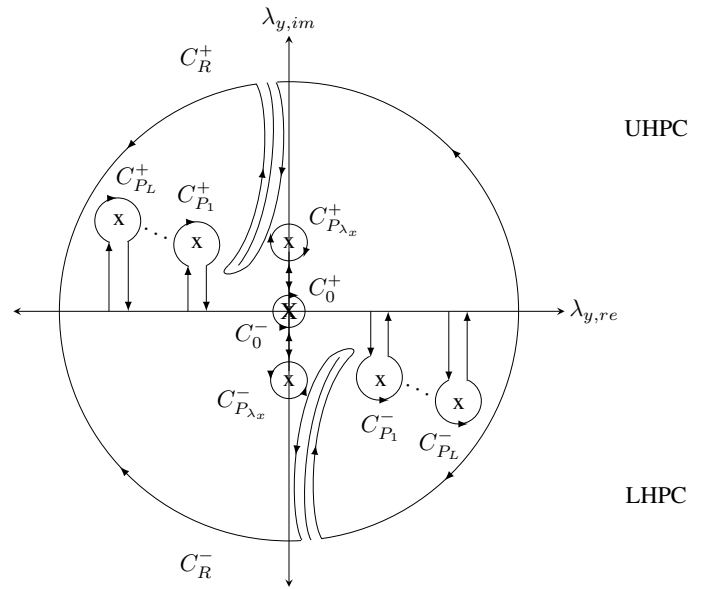


Figure 2: The integrand of (25) in the complex λ_y plane. The branch cut arises from the square root term in $\lambda_{z\theta}$ and is removable due to the fact that the integrand is even in $\lambda_{z\theta}$. Note that the distance between the paths around the singularities are exaggerated to give a better view of the overall contour path for implementing CIT. In reality, they lie on top of each other.

contribution and the TM^z UHP and LHP contributions and combining the results yields

$$A_{vw}^{(11)} = \frac{\delta_{vw}}{Z_v Z_w} - \frac{Z_w}{4} \left\{ \int_{-\infty}^{\infty} C_{\lambda_x} \left[A_{\lambda_y}^{(11)} + B_{\lambda_y}^{(11)} \right. \right. \\ \left. \left. + C_{\lambda_y}^{(11)} + D_{\lambda_y}^{(11)} \right] d\lambda_x \right\} \quad (29)$$

where

$$C_{\lambda_x} = \left[\frac{(1 - (-1)^{m_v} e^{j\lambda_x a}) (1 - (-1)^{m_w} e^{-j\lambda_x a})}{(\lambda_x + k_{xv})(\lambda_x - k_{xv})(\lambda_x + k_{xw})(\lambda_x - k_{xw})} \right] \quad (30)$$

In (30),

$$A_{\lambda_y}^{(11)} = \left(\frac{M_{hx}^v M_{hx}^w m_v m_w}{a^2} \right) \left\{ \frac{j2\pi b \lambda_{z\theta}^* \left[\frac{\cos(\lambda_{z\theta}^* d)}{\sin(\lambda_{z\theta}^* d)} \right]}{\omega \mu_t} \right. \\ - \frac{4\pi \mu_z \lambda_x^2}{\omega \mu_t^2 d} \sum_{l=0}^{\infty} \left(\frac{\pi l}{d} \right)^2 \frac{(1 - e^{-j\lambda_{y1\theta} b})}{\lambda_{y1\theta}^3 (\lambda_{y1\theta}^2 + \lambda_x^2)} \\ \left. - \frac{4\pi \omega \varepsilon_z}{d} \sum_{l=0}^{\infty} \frac{(1 - e^{-j\lambda_{y1\psi} b})}{\lambda_{y1\psi} (\lambda_{y1\psi}^2 + \lambda_x^2) [1 + \delta_{0,l}]} \right\},$$

$$B_{\lambda_y}^{(11)} = C_{\lambda_y}^{(11)} = D_{\lambda_y}^{(11)} = 0 \quad (31)$$

where

$$\lambda_{y_{l\theta}} = \sqrt{\mu_z/\mu_t \left[k_t^2 - (l\pi/d)^2 \right] - \lambda_x^2} \quad (32)$$

$$\lambda_{y_{l\psi}} = \sqrt{\varepsilon_z/\varepsilon_t \left[k_t^2 - (l\pi/d)^2 \right] - \lambda_x^2} \quad (33)$$

$$\lambda_{z\theta}^* = \sqrt{k_t^2 - \mu_t/\mu_z \lambda_x^2}. \quad (34)$$

The A^{11} term for the other four cases as well as the other MoM matrix elements (i.e., A^{12} , A^{21} , and A^{22}) are evaluated in a similar manner.

Although evaluating these integrals is onerous, the gain in terms of code efficiency is significant, especially when considering a large number of modes in the MoM solution.¹ Finally, note that a branch cut appears in the λ_x complex plane through the terms $\lambda_{z\theta}^*$, $\lambda_{y_{l\theta}}$, and $\lambda_{y_{l\psi}}$. Since the integrand is not even in those terms, the branch cut contribution is *not* removable. Therefore, as mentioned previously, the λ_x integral is evaluated numerically.

III. VALIDATION

A. Experimental configuration

Material measurements were made using the configuration shown in Fig. 3, capturing both the transmission and reflection measurements from an Agilent Technologies E8362B PNA. The clamped waveguide configuration consisted of 15.24 cm \times 15.24 cm \times 0.635 cm (6 in. \times 6 in. \times 0.25 in.) aluminum flanges attached using precision alignment pins and screws to two Maury Microwave precision X-band waveguides. The waveguides were mounted on a stable platform using optical table components and custom machined waveguide clamps, providing excellent repeatability and precision during the measurement process.

The system was calibrated using the well-known Thru-Reflect-Line [23] technique, which is conducted using the built-in calibration routine of the PNA. Here, the thru measurement was made with the rectangular waveguides connected to the flange plates, which were then clamped together. For the reflect measurement, a highly reflective brass plate was placed between the flanges. Since the typical line standard would require precise custom fabrication, the normal $\lambda/4$ line standard was replaced with a modified measurement, in which the two rectangular waveguides were directly connected and a negative phase delay of 43.730ps was manually entered to compensate for the thickness of the two 0.635 cm (0.25 in.) flange plates. This time delay correlates to the thickness of the plates.

For the plots, error bars take into consideration uncertainties in the real and imaginary parts of each of the S -parameters and the thickness of the material. Therefore, we have the

¹This is simply a factor of evaluating fewer integrals, as numerical integration is computationally expensive. In the most extreme cases, the nonlinear least squares solver will require dozens of function evaluations at each frequency to converge; therefore, calculating 1 integral numerically is significantly more efficient than calculating 4.

uncertainty for a given solution at a single frequency value as:

$$\begin{aligned} \sigma_\alpha^2 = & \sum_{i=1}^2 \sum_{j=1}^2 \left[\sigma_{S_{ij,\text{real}}} \left(\frac{\partial \alpha}{\partial S_{ij,\text{real}}} \right) \right]^2 \\ & + \sum_{i=1}^2 \sum_{j=1}^2 \left[\sigma_{S_{ij,\text{imag}}} \left(\frac{\partial \alpha}{\partial S_{ij,\text{imag}}} \right) \right]^2 \\ & + \sum_{k=1}^2 \left[\sigma_{d_k} \left(\frac{\partial \alpha}{\partial d_k} \right) \right]^2 \quad \dots \alpha = \varepsilon_t, \varepsilon_z \mu_t, \mu_z \end{aligned} \quad (35)$$

In the absence of analytical expressions for the required partial derivatives, we compute the approximate numerical derivatives using the finite difference formula, with h a small change:

$$\frac{\partial f(x)}{\partial x} = \frac{f(x+h) - f(x)}{h} \quad (36)$$

Previous work has shown that material thickness is the largest contributor to uncertainty [17]. All errors bars are plotted as $\pm 2\sigma$.

Because the constitutive parameters are still contained in a complex integral over λ_x , a non-linear least squares method, in particular, MATLAB®'s *lsqcurvefit*, is utilized to extract the constitutive parameters. This algorithm is based on the Trust Region Reflective (TRR) method and is not overly sensitive to the initial guess, based on the experience gained through previous work and MATLAB® documentation. However, it should be noted that this method requires a number of iterations to converge, which can increase computation time. In order to minimize the impact of convergence time, the code updates its initial guess based on previous values. This leads to more rapid convergence over the frequencies under consideration. Furthermore, it is well known that nonlinear least squares methods are sensitive to outliers. This paper takes accurate and precise calibration as the most practical remedy.

In order to test the validity of the code, the method was utilized to extract permittivity and permeability (by assuming $\varepsilon_t = \varepsilon_z$ and $\mu_t = \mu_z$) on isotropic materials; the results showed excellent agreement with well-known methods, such as Nicholson-Ross-Weir. This provided good confidence to proceed with uniaxial materials.

B. Experimental results

1) *Characterization of 3D-printed honeycomb*: Materials with occlusions arranged in a lattice structure (such as honeycomb) can be expected to demonstrate uniaxial characteristics. With recent advances in 3D printing technology and ease of access to such devices, patterned materials can be generated in CAD software and rapid prototyping of engineered materials is a fairly simple matter. In the course of this work, a Connex 500 was used for producing prototype materials. The "ink" used in the printer was a white nylon polymer and was utilized to make a honeycomb patterned material. Due to resource

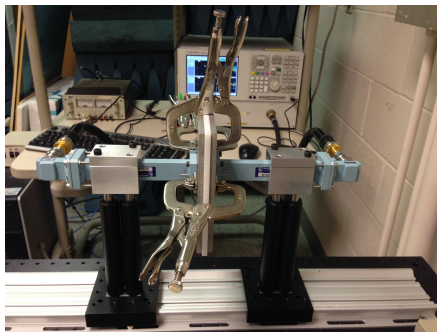


Figure 3: The tFWMT apparatus shown measuring a white nylon material. The tFWMT is supported in a mounting platform and clamps are used to ensure good contact between the MUT and the flange plates. The mounting platform and the clamps allow for excellent repeatability and precision in the measurement process.

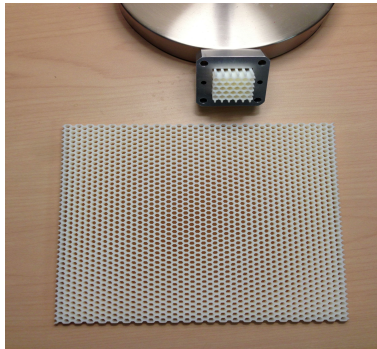


Figure 4: Samples of the honeycomb material used for the tFWMT and WRWS measurements. The center-to-vertex spacing of each regular hexagonal cell was 1.7 mm. The center-to-center spacing of each cell was 3.5 mm.

limitations, the white nylon polymer was the only material available for use in the 3D printer. Therefore, the occlusions of the prototype materials consisted of air. As a result, the measurements in the rest of this paper are limited to non-magnetic uniaxial materials.

Due to the low-loss nature of the lattice material and the air-filled hexagonal cells, the measured S -parameters were time-gated to eliminate the reflections from the edges of the plates using the method described in [17]. A photograph of the 3D-printed honeycomb samples is shown in Fig. 4. In order to compare the values extracted via the tFWMT, the method described in [24]–[26] was used to extract the permittivity. This technique, called the waveguide rectangular to waveguide square (WRWS) technique, utilized a waveguide that slowly tapers from the standard X-band aperture to a square aperture, allowing for the measurement of a precisely cut cube sample. In this case, the sample was measured at orthogonal orientations and the values were extracted using an iterative root finding method. The WRWS ϵ_t and ϵ_z results are shown in Figs. 5 and 6.

Figure 5 shows the dominant-mode-only results using the

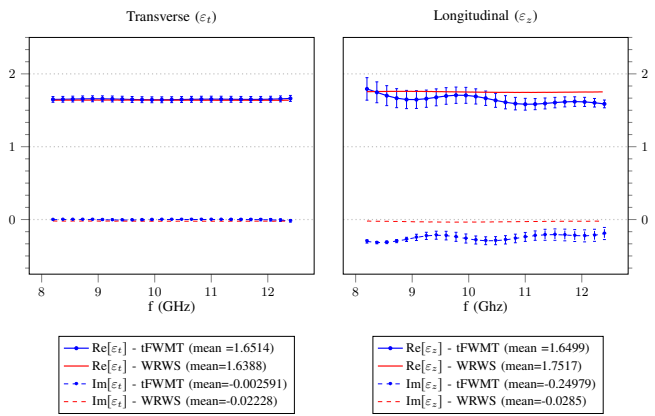


Figure 5: The results from the tFWMT extraction performed on the honeycomb material using only the dominant mode.

tFWMT on the 3D-printed honeycomb sample. It is clear from Fig. 5 that the results for the transverse permittivity ϵ_t agree very well with the WRWS method. The longitudinal permittivity ϵ_z is not as stable nor as well in agreement with WRWS results as the ϵ_t results. This is somewhat expected considering the measurement configuration. In a rectangular waveguide probe, the dominant mode is TE_{10}^z , which does not contain a z -directed electric field component; thus, the tFWMT weakly interrogates ϵ_z . Even so, the tFWMT configuration produces improved results over those reported using a similar nondestructive measurement geometry, where, in some cases, the ϵ_z were not reported due to their instability [9].

With regards to the inclusion of higher-order modes, the authors of [9] hypothesize that higher-order modes do not significantly affect the results for anisotropic materials. Figure 6 demonstrates the results when higher-order modes are considered. In this case, due to the symmetry of the apertures and for computational efficiency, only $\text{TE}_{1(2q)}^z$ and $\text{TM}_{1(2q)}^z$ (where $q = 0, 1, 2, \dots, Q$) are considered [5]. From these results, it is apparent that higher-order modes do not significantly affect the extracted values for ϵ_t , but including the TE_{12}^z and TM_{12}^z modes does elicit a significant change on the $\text{Im}[\epsilon_z]$ results — bringing the values much closer to the WRWS results. Including the higher order modes does produce a significant change in the $\text{Re}[\epsilon_z]$ results, but it is not clear that these results are improved over the dominant-mode-only results. Therefore, it is difficult to draw concrete conclusions from the data at hand about the validity of the hypothesis that dominant-mode-only analysis is sufficiently accurate for most applications. Note that additional modes beyond these two do not contribute significantly to either component.

2) *Characterization of lossy honeycomb:* A uniform insertion loss carbon-loaded honeycomb core was procured from Cuming Microwave. The cells were manufactured with 0.3175 cm (0.125 in.) width and the core was loaded with a proprietary lossy coating rated at 10 dBi/inch. Since the material is available in 30.48 cm \times 30.48 cm \times 1.02 cm (12 in. \times 12 in. \times 0.4 in.) sheets, a free-space measurement was determined to be the most effective comparison method. The results from the

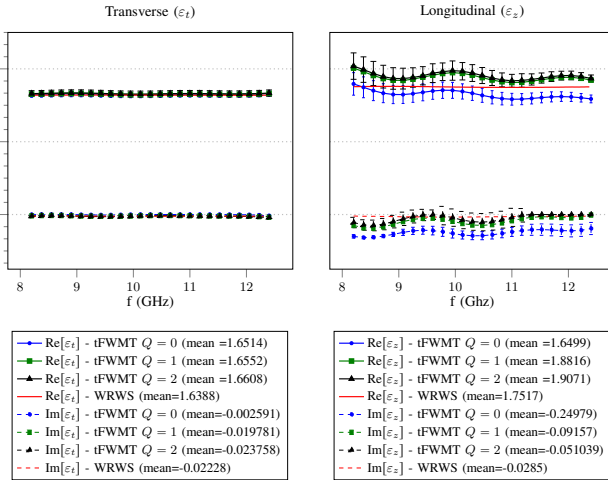


Figure 6: The results from the tFWMT extraction performed on the honeycomb material incorporating higher-order modes. Only the $TE_{1(2q)}^z$ and $TM_{1(2q)}^z$ modes are considered for $Q = 0, 1,$ and 2 .

focused beam measurement technique (FBMT) were obtained from measurements made at two different angles of incidence, $\theta_i = 0^\circ$ and 60° .

Figures 7 and 8 plot the results of the extractions. The agreement between the tFWMT and FBMT results for ε_t is quite excellent. Similar to the low-loss honeycomb material results, the agreement between the tFWMT and reference results in the ε_z case is not as good. This conflict is likely due to the measurement configuration limitation discussed above and noted by other researchers [9]. Another source of this disagreement is the inhomogeneity of the sample. Like resistive cards, carbon black was used in the manufacture of the 10 dBi/inch lossy honeycomb material. It is very difficult to ensure uniform loading of the carbon black. This issue is well documented [27]–[30]. Additionally, the slopes of the curves for the ε_z parameters indicate that the honeycomb material is slightly dispersive in the z -direction, which would not be unexpected for a uniaxial structure. This behavior is also seen in [31] for similar types of carbon black-based materials. Therefore, since the z -directed electric field interrogates the carbon black walls more strongly than the transverse electric field, the effect is more pronounced in the results for ε_z .

IV. SIMULATION OF HIGHER PERMITTIVITY MATERIALS

In order to more fully characterize the method’s utility, the materials described in [32] were simulated in the tFWMT configuration and results compared to Knisely’s work. The measurement methods utilized in [32] are the Single Port Waveguide Probe (SPWP) method, and the usual Rectangular Waveguide (RWG) method for comparison. The SPWP method differs from the tFWMT only in that one waveguide probe is replaced with a PEC sheet. Since the SPWP provides a smaller number of measurements, its utility is inherently more limited in fully characterizing complex materials. This paper considers two simulated uniaxial materials for comparison –

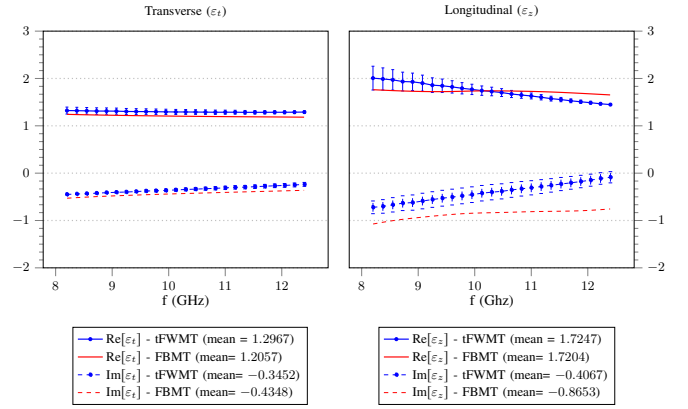


Figure 7: The results from the tFWMT extraction performed on the lossy 10 dBi/inch honeycomb material using only the dominant mode. The errors bars are $\pm 2\sigma$.

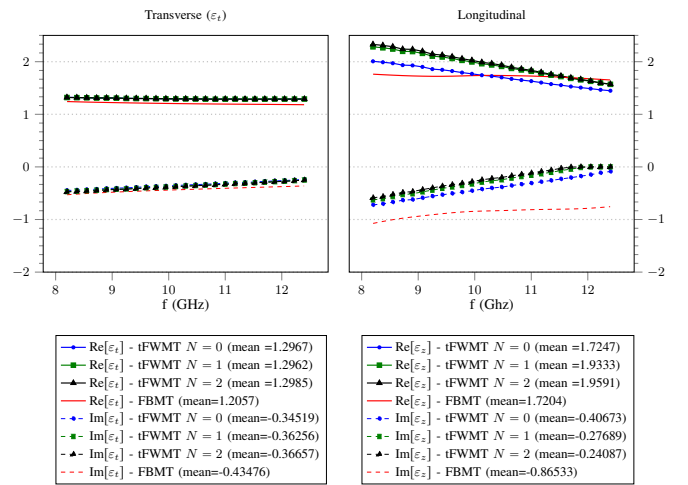


Figure 8: The results from the tFWMT extraction performed on the lossy 10 dBi/inch honeycomb material incorporating higher-order modes. Only the $TE_{1(2n)}^z$ and $TM_{1(2n)}^z$ modes are considered for $n = 0, 1,$ and 2 . Error bars are omitted for visual simplicity.

a high contrast material and a single slab uniaxial material. All simulations were full wave and run using CST Microwave Studio.

A. High Contrast Simulated Material

The high contrast simulated material is composed of a slab material with a specified permittivity of $2.5 - j0.2$ incorporating tetragonal inclusions comprised of a material with a specified permittivity of $9.9 - j0.0$. Each simulation is calibrated by means of a Thru-Reflect-Line (TRL) method. Results of the comparison are shown in Figure 9. The results demonstrate similar behavior as with the lossy honeycomb material shown in Figure 6, to include the periodic shape of the longitudinal (ε_z) permittivity curves.

In order to provide one further point of comparison, a single slab of uniaxial material with known dispersive permittivities,

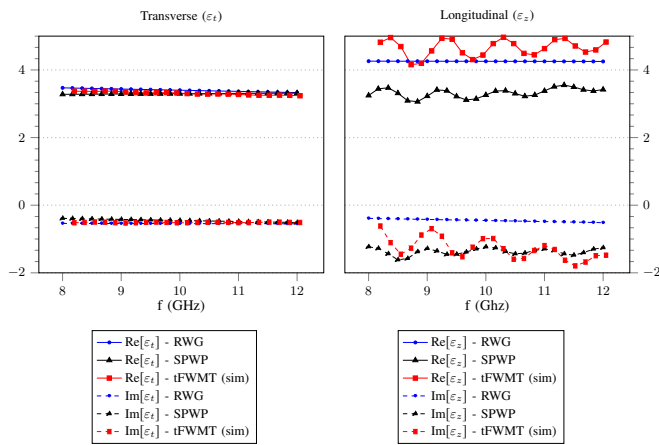


Figure 9: A comparison of extraction results, using the high contrast uniaxial material described in [32]. The Rectangular Waveguide Probe (RWG) and Single Port Waveguide Probe (SPWP) results are directly from the referenced paper, while the tFWMT results utilized the same simulated material in a tFWMT simulation, performed in CST. The tFWMT was then employed to extract permittivities from the resulting S-Parameters. Only the $TE_{1(2n)}^z$ and $TM_{1(2n)}^z$ modes are considered for $n = 0, 1, \text{ and } 2$. Error bars are omitted for visual simplicity.

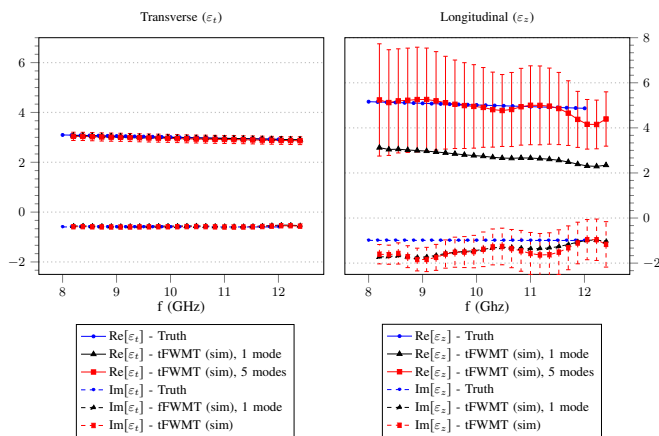


Figure 10: A comparison of extraction results using the high contrast sample of [32]. In this case, instead of modeling the physical structure of the material, a solid 0.125 inch slab of material with known uniaxial parameters was simulated in the tFWMT geometry, again using CST. Only the $TE_{1(2n)}^z$ and $TM_{1(2n)}^z$ modes are considered for $n = 0, 1, \text{ and } 2$. In this case, the error bars are displayed to highlight the large uncertainty.

ϵ_t and ϵ_z , similar to the high contrast material, were simulated in the tFWMT configuration. The results demonstrate similar behavior to both previous lab and simulation cases for lossy, high permittivity materials, including a higher uncertainty. This higher uncertainty was determined to be associated with the S_{12} and S_{21} parameters, which further confirms that this behavior is due to a weak interrogating field in the z -direction.

V. CONCLUSIONS

The primary focus of this work was to develop and demonstrate a method for the simultaneous nondestructive extraction of the permittivity and permeability of a uniaxial anisotropic media. The method utilized a single fixture in which the MUT is clamped between two flanged rectangular waveguides. The transmission and reflection coefficients were measured and then compared with the theoretical coefficients to find $\vec{\epsilon}$ via nonlinear least squares. Both low-loss and lossy uniaxial honeycomb materials were measured using this configuration, and simulations performed to correlate the results to previously published works. The results for real part of the transverse permittivity were shown to converge to a stable solution utilizing the dominant mode TE_{10}^z , while the imaginary part is shown to converge with the addition of one higher-order mode, the TE_{12}^z and TM_{12}^z hybrid mode. As expected, the extracted transverse constitutive parameters were in good agreement with traditional destructive methods. The new technique produced good, but mildly unstable values when extracting the longitudinal parameters, as a result of a weak z -directed electric field component.

With regards to the inclusion of higher order modes, we see acceptable convergence to a stable solution for the extracted longitudinal permittivity values when including two additional modes. This is likely due to the presence of a z -directed electric field in the higher order modes. Regardless of this limitation, this work is a significant contribution to the scientific community because the results are a significant improvement over previous nondestructive methods for anisotropic materials. Therefore, it is recommended to further test this method on a wider range of materials, including both dielectric and magnetic uniaxial materials, in order to assess the precision of the method to simultaneously extract permeability and permittivity.

Furthermore, we note the two physical MUTs considered in this paper varied in thickness from 0.25" to 0.4". As noted in [5], thicker materials are more accurately measured when including higher order modes in the MFIEs. This was indeed the case, as measurement of a thinner, low-loss honeycomb showed good agreement while only including the dominant mode. However, the thicker, lossy honeycomb material required inclusion of higher order modes to show better agreement with the reference methods.

Finally extraction of ϵ_t , ϵ_z , μ_t , and μ_z requires another set of independent measurements, which was not performed due to limited material availability. However, future work could focus on incorporating additional set of independent measurements (such as the TTM) for extraction of a larger number of parameters. Additionally, it is possible that utilizing a slightly different configuration, where the waveguides are placed next to one another and the MUT is backed by a sheet of PEC [7], [27], will allow for improvements in crack and defect detection of advanced materials, when access is limited to a single side of the MUT.

REFERENCES

- [1] R. K. Kawakami, E. J. Escorcía-Aparicio, and Z. Q. Qiu, "Symmetry-induced magnetic anisotropy in Fe films grown on stepped Ag(001)," *Phys. Rev. Lett.*, vol. 77, pp. 2570–2573, Sep 1996. [Online]. Available: <https://link.aps.org/doi/10.1103/PhysRevLett.77.2570>
- [2] D. Gay, *Composite materials: design and applications*. CRC press, 2014.
- [3] C. Chang, K. Chen, and J. Qian, "Nondestructive determination of electromagnetic parameters of dielectric materials at X-band frequencies using a waveguide probe system," *IEEE Transactions Instrumentation Measurement*, vol. 46, no. 5, pp. 1084–1092, 1997.
- [4] G. D. Dester, E. J. Rothwell, and M. J. Havrilla, "Two-iris method for the electromagnetic characterization of conductor-backed absorbing materials using an open-ended waveguide probe," *IEEE Transactions on Instrumentation and Measurement*, vol. 61, no. 4, pp. 1037–1044, 2012.
- [5] M. W. Hyde and M. J. Havrilla, "A nondestructive technique for determining complex permittivity and permeability of magnetic sheet materials using two flanged rectangular waveguides," *Progress in Electromagnetics Research*, vol. 79, pp. 367–386, 2008.
- [6] N. Maode, S. Yong, Y. Jinkui, F. Chenpeng, and X. Deming, "An improved open-ended waveguide measurement technique on parameters ϵ_r and μ_r of high-loss materials," *IEEE Transactions Instrumentation Measurement*, vol. 47, no. 2, pp. 476–481, 1998.
- [7] J. Stewart and M. Havrilla, "Electromagnetic characterization of a magnetic material using an open-ended waveguide probe and a rigorous full-wave multimode model," *JEWA*, vol. 20, no. 14, pp. 2037–2052, 2006.
- [8] M. D. Seal, M. W. Hyde, and M. J. Havrilla, "Nondestructive complex permittivity and permeability extraction using a two-layer dual-waveguide probe measurement geometry," *Progress in Electromagnetics Research*, vol. 123, pp. 123–142, 2012.
- [9] C. Chang, K. Chen, and J. Qian, "Nondestructive measurements of complex tensor permittivity of anisotropic materials using a waveguide probe system," *IEEE Transactions Microwave Theory Techniques*, vol. 44, no. 7, pp. 1081–1090, 1996.
- [10] J. Krupka, K. Derzakowski, A. Abramowicz, M. Tobar, and R. Geyer, "Use of whispering-gallery modes for complex permittivity determinations of ultra-low-loss dielectric materials," *IEEE Transactions on Microwave Theory Techniques*, vol. 47, no. 6, pp. 752–759, 1999.
- [11] Y. Xu, "A study of waveguides filled with anisotropic metamaterials," *Microwave Optics Technology Letters*, vol. 41, no. 5, pp. 426–431, 2004.
- [12] D. Smith, D. Vier, T. Koschny, and C. Soukoulis, "Electromagnetic parameter retrieval from inhomogeneous metamaterials," *Physical Review E*, vol. 71, no. 3, 2005.
- [13] G. Mumcu, K. Sertel, and J. Volakis, "A measurement process to characterize natural and engineered low-loss uniaxial dielectric materials at microwave frequencies," *IEEE Transactions on Microwave Theory Techniques*, vol. 56, no. 1, pp. 217–223, 2008.
- [14] Z. Li, K. Aydin, and E. Ozbay, "Determination of the effective constitutive parameters of bianisotropic metamaterials from reflection and transmission coefficients," *Physical Review E*, vol. 79, no. 2, 2009.
- [15] B. Crowgey, J. Tang, O. Tuncer, L. Kempel, E. Rothwell, and B. Shanker, "Measurement of anisotropic material properties for antenna applications," in *Proceedings of Antennas and Propagation Conference (LAPC)*, 2012, pp. 1–4.
- [16] J. Schultz, *Focused Beam Methods: Measuring Microwave Materials in Free Space*. Createspace Independent Publishing, 2012.
- [17] M. Hyde, M. Havrilla, and A. Bogle, "A novel and simple technique for measuring low-loss materials using the two flanged waveguides measurement geometry," *Measurement Science Technology*, vol. 22, no. 8, 2011.
- [18] M. W. Hyde IV, M. J. Havrilla, and A. E. Bogle, "Nondestructive determination of the permittivity tensor of a uniaxial material using a two-port clamped coaxial probe," *IEEE Transactions on Microwave Theory and Techniques*, vol. 64, no. 1, pp. 239–246, Jan 2016.
- [19] J. Baker-Jarvis, M. D. Janezic, P. D. Domich, and R. G. Geyer, "Analysis of an open-ended coaxial probe with lift-off for nondestructive testing," *IEEE Transactions on Instrumentation and Measurement*, vol. 43, no. 5, pp. 711–718, 1994.
- [20] R. Collin, *Field Theory of Guided Waves*. IEEE Press, 1991.
- [21] N. Rogers, "Nondestructive electromagnetic characterization of uniaxial materials," Ph.D. dissertation, Air Force Institute of Technology, 2014.
- [22] N. Rogers and M. Havrilla, "Dyadic green's functions for a parallel plate waveguide filled with anisotropic uniaxial media," *Progress In Electromagnetics Research B*, vol. 63, pp. 249–261, 2015.
- [23] G. F. Engen and C. A. Hoer, "Thru-reflect-line: an improved technique for calibrating the dual six-port automatic network analyzer," *IEEE Transactions Microwave Theory Techniques*, vol. 27, no. 12, pp. 987–993, 1979.
- [24] A. Knisely, M. Havrilla, P. Collins, M. Hyde, J. Allen, A. Bogle, and E. Rothwell, "Biaxial anisotropic material characterization using rectangular to square waveguide," in *36th Annual Symposium of the Antenna Measurement Techniques Association Conference Proceedings*, 2014, pp. 437–442.
- [25] A. Knisely and M. Havrilla, "Material characterization de-embedding for rectangular to square waveguide," in *2015 9th European Conference on Antennas and Propagation (EuCAP)*. IEEE, 2015, pp. 1–5.
- [26] A. Knisely, M. Havrilla, and M. Hyde, "Material characterization uncertainty analysis for rectangular to square waveguide," in *2015 IEEE AP-S Symposium on Antennas and Propagation and URSI USNC-CNC Joint Meeting*. IEEE, 2015, pp. 98–98.
- [27] M. Hyde IV, J. Stewart, M. Havrilla, W. Baker, E. Rothwell, and D. Nyquist, "Nondestructive electromagnetic material characterization using a dual waveguide probe: A full wave solution," *Radio Science*, vol. 44, no. 3, p. RS3013, 2009.
- [28] B. B. Glover, K. W. Whites, M. W. Hyde IV, and M. J. Havrilla, "Complex effective permittivity of carbon loaded dielectric films with printed metallic square rings," in *Proceedings of 2nd International Congress on Advanced Electromagnetic Materials in Microwaves and Optics (Metamaterials '2008)*, 2008, pp. 762–764.
- [29] F. Costa, "Surface impedance measurement of resistive coatings at microwave frequencies," *IEEE Transactions Instrumentation Measurement*, vol. 62, no. 2, pp. 432–437, 2013.
- [30] J. Massman, M. Havrilla, K. Whites, and M. Hyde, "A stepped flange waveguide technique for determining tapered R-card sheet impedance," in *Proceedings of the Asia-Pacific Microwave Conference (APMC)*, Dec. 2010, pp. 1769–1772.
- [31] M. Hotta, M. Hayashi, M. T. Lanagan, D. K. Agrawal, and K. Nagata, "Complex permittivity of graphite, carbon black and coal powders in the ranges of x-band frequencies (8.2 to 12.4 GHz) and between 1 and 10 GHz," *ISIJ International*, vol. 51, no. 11, pp. 1766–1772, 2011.
- [32] A. G. Knisely, M. W. Hyde, M. J. Havrilla, and P. J. Collins, "Uniaxial anisotropic material measurement using a single port waveguide probe," in *AMTA 2016 Proceedings*. IEEE, 2016, pp. 1–6.



Neil Rogers Received the B.S. degree in electrical engineering from the University of Tulsa, Tulsa, OK, in 2003 and the M.S. and Ph.D. degrees in electrical engineering from the Air Force Institute of Technology, Wright-Patterson Air Force Base, Dayton, OH, in 2009 and 2014, respectively. From 2003-2007, he was an Acquisitions Officer at the National Air and Space Intelligence Center, Wright-Patterson Air Force Base, OH. From 2009-2011, he was a Government Researcher with the Air Force Research Laboratory, Kirtland Air Force Base, NM.

From 2014-2018, he served as the Deputy Chief Engineer for the JSTARS Recap program at Hanscom Air Force Base, MA. He is currently an Associate Professor of Electrical Engineering at the United States Air Force Academy. His current research interests include electromagnetic material characterization, radar mode development, and electromagnetic scattering and propagation. Dr. Rogers is a member of the Eta Kappa Nu and Tau Beta Pi honor societies.



Michael Havrilla (S'85–M'86–SM'05) received B.S. degrees in physics and mathematics, the M.S.E.E degree, and the Ph.D. degree in electrical engineering from Michigan State University, East Lansing, MI, in 1987, 1989, and 2001, respectively. From 1990 to 1995, he was with General Electric Aircraft Engines, Evendale, OH and Lockheed Skunk Works, Palmdale, CA, where he worked as an Electrical Engineer. He is currently an Associate Professor in the Department of Electrical and Computer Engineering at the Air Force Institute of

Technology, Wright-Patterson AFB, OH. His current research interests include electromagnetic and guided-wave theory, electromagnetic propagation and radiation in complex media and structures and electromagnetic materials characterization. Dr. Havrilla is a member of URSI Commission B and the Eta Kappa Nu and Sigma Xi honor societies.



Milo W. Hyde IV (S'10—M'10—SM'12) received the B.S. degree in computer engineering from the Georgia Institute of Technology, Atlanta, GA in 2001 and the M.S. and Ph.D. degrees in electrical engineering from the Air Force Institute of Technology, Wright-Patterson Air Force Base (WPAFB), Dayton, OH in 2006 and 2010, respectively. From 2001 to 2004, he was a maintenance officer with the F-117A Nighthawk, Holloman AFB, Alamogordo, NM. From 2006 to 2007, he was a government researcher with the Air Force Research Laboratory,

WPAFB. He is currently an Associate Professor in the Department of Electrical and Computer Engineering at the Air Force Institute of Technology. His current research interests include electromagnetic material characterization, guided-wave theory, scattering, and optics. Dr. Hyde is a member of the International Society for Optical Engineering, the Optical Society of America, the American Geophysical Union, the Directed Energy Professional Society, and the Applied Computational Electromagnetics Society.



Alex Knisely Alexander Knisely received his B.S. Degree in electrical engineering from Wright State University, Dayton, OH in 2012 and his M.S. Degree in electrical engineering from the Air Force Institute of Technology (AFIT), Wright-Patterson Air Force Base, OH in 2015. He is currently an electrical engineering Ph.D. Candidate at AFIT. His current research interests include electromagnetic material characterization, guided-wave theory, and electromagnetic propagation and radiation in complex media and structures.